

First all-sky search for continuous gravitational waves from unknown sources in binary systems

J. Aasi,¹ B. P. Abbott,¹ R. Abbott,¹ T. Abbott,² M. R. Abernathy,¹ T. Accadia,³ F. Acernese,^{4,5} K. Ackley,⁶ C. Adams,⁷ T. Adams,⁸ P. Addresso,⁵ R. X. Adhikari,¹ C. Affeldt,⁹ M. Agathos,¹⁰ N. Aggarwal,¹¹ O. D. Aguiar,¹² A. Ain,¹³ P. Ajith,¹⁴ A. Alemeic,¹⁵ B. Allen,^{9,16,17} A. Allocca,^{18,19} D. Amariutei,⁶ M. Andersen,²⁰ R. Anderson,¹ S. B. Anderson,¹ W. G. Anderson,¹⁶ K. Arai,¹ M. C. Araya,¹ C. Arceneaux,²¹ J. Areeda,²² S. M. Aston,⁷ P. Astone,²³ P. Aufmuth,¹⁷ C. Aubert,⁹ L. Austin,¹ B. E. Aylott,²⁴ S. Babak,²⁵ P. T. Baker,²⁶ G. Ballardin,²⁷ S. W. Ballmer,¹⁵ J. C. Barayoga,¹ M. Barbet,⁶ B. C. Barish,¹ D. Barker,²⁸ F. Barone,^{4,5} B. Barr,²⁹ L. Barsotti,¹¹ M. Barsuglia,³⁰ M. A. Barton,²⁸ I. Bartos,³¹ R. Bassiri,²⁰ A. Basti,^{18,32} J. C. Batch,²⁸ J. Bauchrowitz,⁹ Th. S. Bauer,¹⁰ B. Behnke,²⁵ M. Bejger,³³ M. G. Beker,¹⁰ C. Belczynski,³⁴ A. S. Bell,²⁹ C. Bell,²⁹ G. Bergmann,⁹ D. Bersanetti,^{35,36} A. Bertolini,¹⁰ J. Betzwieser,⁷ P. T. Beyersdorf,³⁷ I. A. Bilenko,³⁸ G. Billingsley,¹ J. Birch,⁷ S. Biscans,¹¹ M. Bitossi,¹⁸ M. A. Bizouard,³⁹ E. Black,¹ J. K. Blackburn,¹ L. Blackburn,⁴⁰ D. Blair,⁴¹ S. Bloemen,^{42,10} M. Blom,¹⁰ O. Bock,⁹ T. P. Bodiya,¹¹ M. Boer,⁴³ G. Bogaert,⁴³ C. Bogan,⁹ C. Bond,²⁴ F. Bondu,⁴⁴ L. Bonelli,^{18,32} R. Bonnand,⁴⁵ R. Bork,¹ M. Born,⁹ V. Boschi,¹⁸ Sukanta Bose,^{46,13} L. Bosi,⁴⁷ C. Bradaschia,¹⁸ P. R. Brady,¹⁶ V. B. Braginsky,³⁸ M. Branchesi,^{48,49} J. E. Brau,⁵⁰ T. Briant,⁵¹ D. O. Bridges,⁷ A. Brillet,⁴³ M. Brinkmann,⁹ V. Brisson,³⁹ A. F. Brooks,¹ D. A. Brown,¹⁵ D. D. Brown,²⁴ F. Brückner,²⁴ S. Buchman,²⁰ T. Bulik,³⁴ H. J. Bulten,^{10,52} A. Buonanno,⁵³ R. Burman,⁴¹ D. Buskulic,³ C. Buy,³⁰ L. Cadonati,⁵⁴ G. Cagnoli,⁴⁵ J. Calderón Bustillo,⁵⁵ E. Calloni,^{4,56} J. B. Camp,⁴⁰ P. Campsie,²⁹ K. C. Cannon,⁵⁷ B. Canuel,²⁷ J. Cao,⁵⁸ C. D. Capano,⁵³ F. Carbognani,²⁷ L. Carbone,²⁴ S. Caride,⁵⁹ A. Castiglia,⁶⁰ S. Caudill,¹⁶ M. Cavaglia,²¹ F. Cavalier,³⁹ R. Cavalieri,²⁷ C. Celerier,²⁰ G. Cella,¹⁸ C. Cepeda,¹ E. Cesarini,⁶¹ R. Chakraborty,¹ T. Chalermongsak,¹ S. J. Chamberlin,¹⁶ S. Chao,⁶² P. Charlton,⁶³ E. Chassande-Mottin,³⁰ X. Chen,⁴¹ Y. Chen,⁶⁴ A. Chincarini,³⁵ A. Chiummo,²⁷ H. S. Cho,⁶⁵ J. Chow,⁶⁶ N. Christensen,⁶⁷ Q. Chu,⁴¹ S. S. Y. Chua,⁶⁶ S. Chung,⁴¹ G. Ciani,⁶ F. Clara,²⁸ J. A. Clark,⁵⁴ F. Cleva,⁴³ E. Coccia,^{68,69} P.-F. Cohadon,⁵¹ A. Colla,^{23,70} C. Collette,⁷¹ M. Colombini,⁴⁷ L. Cominsky,⁷² M. Constancio, Jr.,¹² A. Conte,^{23,70} D. Cook,²⁸ T. R. Corbitt,² M. Cordier,³⁷ N. Cornish,²⁶ A. Corpuz,⁷³ A. Corsi,⁷⁴ C. A. Costa,¹² M. W. Coughlin,⁷⁵ S. Coughlin,⁷⁶ J.-P. Coulon,⁴³ S. Countryman,³¹ P. Couvares,¹⁵ D. M. Coward,⁴¹ M. Cowart,⁷ D. C. Coyne,¹ R. Coyne,⁷⁴ K. Craig,²⁹ J. D. E. Creighton,¹⁶ T. D. Creighton,⁷⁷ S. G. Crowder,⁷⁸ A. Cumming,²⁹ L. Cunningham,²⁹ E. Cuoco,²⁷ K. Dahl,⁹ T. Dal Canton,⁹ M. Damjanic,⁹ S. L. Danilishin,⁴¹ S. D'Antonio,⁶¹ K. Danzmann,^{17,9} V. Dattilo,²⁷ H. Daveloza,⁷⁷ M. Davies,³⁹ G. S. Davies,²⁹ E. J. Daw,⁷⁹ R. Day,²⁷ T. Dayanga,⁴⁶ G. Debreczeni,⁸⁰ J. Degallaix,⁴⁵ S. Deléglise,⁵¹ W. Del Pozzo,¹⁰ T. Denker,⁹ T. Dent,⁹ H. Dereli,⁴³ V. Dergachev,¹ R. De Rosa,^{4,56} R. T. DeRosa,² R. DeSalvo,⁸¹ S. Dhurandhar,¹³ M. Díaz,⁷⁷ L. Di Fiore,⁴ A. Di Lieto,^{18,32} I. Di Palma,⁹ A. Di Virgilio,¹⁸ A. Donath,²⁵ F. Donovan,¹¹ K. L. Dooley,⁹ S. Doravari,⁷ S. Dossa,⁶⁷ R. Douglas,²⁹ T. P. Downes,¹⁶ M. Drago,^{82,83} R. W. P. Drever,¹ J. C. Driggers,¹ Z. Du,⁵⁸ S. Dwyer,²⁸ T. Eberle,⁹ T. Edo,⁷⁹ M. Edwards,⁸ A. Effler,² H. Eggenstein,⁹ P. Ehrens,¹ J. Eichholz,⁶ S. S. Eikenberry,⁶ G. Endrőczi,⁸⁰ R. Essick,¹¹ T. Etzel,¹ M. Evans,¹¹ T. Evans,⁷ M. Factourovich,³¹ V. Fafone,^{61,69} S. Fairhurst,⁸ Q. Fang,⁴¹ S. Farinon,³⁵ B. Farr,⁷⁶ W. M. Farr,²⁴ M. Favata,⁸⁴ H. Fehrmann,⁹ M. M. Fejer,²⁰ D. Feldbaum,^{6,7} F. Feroz,⁷⁵ I. Ferrante,^{18,32} F. Ferrini,²⁷ F. Fidecaro,^{18,32} L. S. Finn,⁸⁵ I. Fiori,²⁷ R. P. Fisher,¹⁵ R. Flaminio,⁴⁵ J.-D. Fournier,⁴³ S. Franco,³⁹ S. Frasca,^{23,70} F. Frasconi,¹⁸ M. Frede,⁹ Z. Frei,⁸⁶ A. Freise,²⁴ R. Frey,⁵⁰ T. T. Fricke,⁹ P. Fritschel,¹¹ V. V. Frolov,⁷ P. Fulda,⁶ M. Fyffe,⁷ J. Gair,⁷⁵ L. Gammatoni,^{47,87} S. Gaonkar,¹³ F. Garufi,^{4,56} N. Gehrels,⁴⁰ G. Gemme,³⁵ E. Genin,²⁷ A. Gennai,¹⁸ S. Ghosh,^{42,10,46} J. A. Giaime,^{7,2} K. D. Giardino,⁷ A. Giazotto,¹⁸ C. Gill,²⁹ J. Gleason,⁶ E. Goetz,^{9,*} R. Goetz,⁶ L. Gondan,⁸⁶ G. González,² N. Gordon,²⁹ M. L. Gorodetsky,³⁸ S. Gossan,⁶⁴ S. Goßler,⁹ R. Gouaty,³ C. Gräf,²⁹ P. B. Graff,⁴⁰ M. Granata,⁴⁵ A. Grant,²⁹ S. Gras,¹¹ C. Gray,²⁸ R. J. S. Greenhalgh,⁸⁸ A. M. Gretarsson,⁷³ P. Groot,⁴² H. Grote,¹⁵ K. Grover,²⁴ S. Grunewald,²⁵ G. M. Guidi,^{48,49} C. Guido,⁷ K. Gushwa,¹ E. K. Gustafson,¹ R. Gustafson,⁵⁹ D. Hammer,¹⁶ G. Hammond,²⁹ M. Hanke,⁹ J. Hanks,²⁸ C. Hanna,⁸⁹ J. Hanson,⁷ J. Harms,¹ G. M. Harry,⁹⁰ I. W. Harry,¹⁵ E. D. Harstad,⁵⁰ M. Hart,²⁹ M. T. Hartman,⁶ C.-J. Haster,²⁴ K. Haughian,²⁹ A. Heidmann,⁵¹ M. Heintze,^{6,7} H. Heitmann,⁴³ P. Hello,³⁹ G. Hemming,²⁷ M. Hendry,²⁹ I. S. Heng,²⁹ A. W. Heptonstall,¹ M. Heurs,⁹ M. Hewitson,⁹ S. Hild,²⁹ D. Hoak,⁵⁴ K. A. Hodge,¹ K. Holt,⁷ S. Hooper,⁴¹ P. Hopkins,⁸ D. J. Hosken,⁹¹ J. Hough,²⁹ E. J. Howell,⁴¹ Y. Hu,²⁹ E. Huerta,¹⁵ B. Hughey,⁷³ S. Husa,⁵⁵ S. H. Huttner,²⁹ M. Huynh,¹⁶ T. Huynh-Dinh,⁷ D. R. Ingram,²⁸ R. Inta,⁸⁵ T. Isogai,¹¹ A. Ivanov,¹ B. R. Iyer,⁹² K. Izumi,²⁸ M. Jacobson,¹ E. James,¹ H. Jang,⁹³ P. Jaranowski,⁹⁴ Y. Ji,⁵⁸ F. Jiménez-Forteza,⁵⁵ W. W. Johnson,² D. I. Jones,⁹⁵ R. Jones,²⁹ R. J. G. Jonker,¹⁰ L. Ju,⁴¹ Haris K,⁹⁶ P. Kalmus,¹ V. Kalogera,⁷⁶ S. Kandhasamy,²¹ G. Kang,⁹³ J. B. Kanner,¹ J. Karlen,⁵⁴ M. Kasprzak,^{27,39} E. Katsavounidis,¹¹ W. Katzman,⁷ H. Kaufer,¹⁷ K. Kawabe,²⁸ F. Kawazoe,⁹ F. Kéfélian,⁴³ G. M. Keiser,²⁰ D. Keitel,⁹ D. B. Kelley,¹⁵ W. Kells,¹ A. Khalaidovski,⁹ F. Y. Khalili,³⁸ E. A. Khazanov,⁹⁷ C. Kim,^{98,93} K. Kim,⁹⁹ N. Kim,²⁰ N. G. Kim,⁹³ Y.-M. Kim,⁶⁵ E. J. King,⁹¹ P. J. King,¹ D. L. Kinzel,⁷ J. S. Kissel,²⁸ S. Klimentenko,⁶ J. Kline,¹⁶ S. Koehlenbeck,⁹ K. Kokeyama,² V. Kondrashov,¹ S. Koranda,¹⁶ W. Z. Korth,¹ I. Kowalska,³⁴ D. B. Kozak,¹ A. Kremin,⁷⁸ V. Kringel,⁹ B. Krishnan,⁹ A. Królak,^{100,101} G. Kuehn,¹⁰² A. Kumar,¹⁵ R. Kumar,²⁹ L. Kuo,⁶² A. Kutynia,¹⁰¹ P. Kwee,¹¹ M. Landry,²⁸ B. Lantz,²⁰ S. Larson,⁷⁶ P. D. Lasky,¹⁰³ C. Lawrie,²⁹ A. Lazzarini,¹ C. Lazzaro,¹⁰⁴ P. Leaci,²⁵ S. Leavey,²⁹ E. O. Lebigot,⁵⁸ C.-H. Lee,⁶⁵ H. K. Lee,⁹⁹ H. M. Lee,⁹⁸ J. Lee,¹¹ M. Leonardi,^{82,83} J. R. Leong,⁹ A. Le Roux,⁷ N. Leroy,³⁹

N. Letendre,³ Y. Levin,¹⁰⁵ B. Levine,²⁸ J. Lewis,¹ T. G. F. Li,^{10,1} K. Libbrecht,¹ A. Libson,¹¹ A. C. Lin,²⁰ T. B. Littenberg,⁷⁶ V. Litvine,¹ N. A. Lockerbie,¹⁰⁶ V. Lockett,²² D. Lodhia,²⁴ K. Loew,⁷³ J. Logue,²⁹ A. L. Lombardi,⁵⁴ M. Lorenzini,^{61,69} V. Lorientte,¹⁰⁷ M. Lormand,⁷ G. Losurdo,⁴⁸ J. Lough,¹⁵ M. J. Lubinski,²⁸ H. Lück,^{17,9} E. Luijten,⁷⁶ A. P. Lundgren,⁹ R. Lynch,¹¹ Y. Ma,⁴¹ J. Macarthur,²⁹ E. P. Macdonald,⁸ T. MacDonald,²⁰ B. Machenschalk,⁹ M. MacInnis,¹¹ D. M. Macleod,² F. Magana-Sandoval,¹⁵ M. Mageswaran,¹ C. Maglione,¹⁰⁸ K. Mailand,¹ E. Majorana,²³ I. Maksimovic,¹⁰⁷ V. Malvezzi,^{61,69} N. Man,⁴³ G. M. Manca,⁹ I. Mandel,²⁴ V. Mandic,⁷⁸ V. Mangano,^{23,70} N. Mangini,⁵⁴ M. Mantovani,¹⁸ F. Marchesoni,^{47,109} F. Marion,³ S. Márka,³¹ Z. Márka,³¹ A. Markosyan,²⁰ E. Maros,¹ J. Marque,²⁷ F. Martelli,^{48,49} I. W. Martin,²⁹ R. M. Martin,⁶ L. Martinelli,⁴³ D. Martynov,¹ J. N. Marx,¹ K. Mason,¹¹ A. Masserot,³ T. J. Massinger,¹⁵ F. Matichard,¹¹ L. Matone,³¹ R. A. Matzner,¹¹⁰ N. Mavalvala,¹¹ N. Mazumder,⁹⁶ G. Mazzolo,^{17,9} R. McCarthy,²⁸ D. E. McClelland,⁶⁶ S. C. McGuire,¹¹¹ G. McIntyre,¹ J. McIver,⁵⁴ K. McLin,⁷² D. Meacher,⁴³ G. D. Meadors,⁵⁹ M. Mehmet,⁹ J. Meidam,¹⁰ M. Meinders,¹⁷ A. Melatos,¹⁰³ G. Mendell,²⁸ R. A. Mercer,¹⁶ S. Meshkov,¹ C. Messenger,²⁹ P. Meyers,⁷⁸ H. Miao,⁶⁴ C. Michel,⁴⁵ E. E. Mikhailov,¹¹² L. Milano,^{4,56} S. Milde,²⁵ J. Miller,¹¹ Y. Minenkov,⁶¹ C. M. F. Mingarelli,²⁴ C. Mishra,⁹⁶ S. Mitra,¹³ V. P. Mitrofanov,³⁸ G. Mitselmakher,⁶ R. Mittleman,¹¹ B. Moe,¹⁶ P. Moesta,⁶⁴ M. Mohan,²⁷ S. R. P. Mohapatra,^{15,60} D. Moraru,²⁸ G. Moreno,²⁸ N. Morgado,⁴⁵ S. R. Morriss,⁷⁷ K. Mossavi,⁹ B. Mours,³ C. M. Mow-Lowry,⁹ C. L. Mueller,⁶ G. Mueller,⁶ S. Mukherjee,⁷⁷ A. Mullavey,² J. Munch,⁹¹ D. Murphy,³¹ P. G. Murray,²⁹ A. Mytidis,⁶ M. F. Nagy,⁸⁰ D. Nanda Kumar,⁶ I. Nardecchia,^{61,69} L. Naticchioni,^{23,70} R. K. Nayak,¹¹³ V. Necula,⁶ G. Nelemans,^{42,10} I. Neri,^{47,87} M. Neri,^{35,36} G. Newton,²⁹ T. Nguyen,⁶⁶ A. Nitz,¹⁵ F. Nocera,²⁷ D. Nolting,⁷ M. E. N. Normandin,⁷⁷ L. K. Nuttall,¹⁶ E. Ochsner,¹⁶ J. O'Dell,⁸⁸ E. Oelker,¹¹ J. J. Oh,¹¹⁴ S. H. Oh,¹¹⁴ F. Ohme,⁸ P. Oppermann,⁹ B. O'Reilly,⁷ R. O'Shaughnessy,¹⁶ C. Osthelder,¹ D. J. Ottaway,⁹¹ R. S. Ottens,⁶ H. Overmier,⁷ B. J. Owen,⁸⁵ C. Padilla,²² A. Pai,⁹⁶ O. Palashov,⁹⁷ C. Palomba,²³ H. Pan,⁶² Y. Pan,⁵³ C. Pankow,¹⁶ F. Paoletti,^{18,27} R. Paoletti,^{18,19} M. A. Papa,^{16,25} H. Paris,²⁸ A. Pasqualetti,²⁷ R. Passaquieti,^{18,32} D. Passuello,¹⁸ M. Pedraza,¹ S. Penn,¹¹⁵ A. Perreca,¹⁵ M. Phelps,¹ M. Pichot,⁴³ M. Pickenpack,⁹ F. Piergiovanni,^{48,49} V. Pierro,^{81,35} L. Pinard,⁴⁵ I. M. Pinto,^{81,35} M. Pitkin,²⁹ J. Poeld,⁹ R. Poggiani,^{18,32} A. Poteomkin,⁹⁷ J. Powell,²⁹ J. Prasad,¹³ S. Premachandra,¹⁰⁵ T. Prestegard,⁷⁸ L. R. Price,¹ M. Prijatelj,²⁷ S. Privitera,¹ R. Prix,⁹ G. A. Prodi,^{82,83} L. Prokhorov,³⁸ O. Puncken,⁷⁷ M. Punturo,⁴⁷ P. Puppó,²³ J. Qin,⁴¹ V. Quetschke,⁷⁷ E. Quintero,¹ G. Quiroga,¹⁰⁸ R. Quitzow-James,⁵⁰ F. J. Raab,²⁸ D. S. Rabeling,^{10,52} I. Rácz,⁸⁰ H. Radkins,²⁸ P. Raffai,⁸⁶ S. Raja,¹¹⁶ G. Rajalakshmi,¹⁴ M. Rakhmanov,⁷⁷ C. Ramet,⁷ K. Ramirez,⁷⁷ P. Rapagnani,^{23,70} V. Raymond,¹ V. Re,^{61,69} J. Read,²² C. M. Reed,²⁸ T. Regimbau,⁴³ S. Reid,¹¹⁷ D. H. Reitze,^{1,6} E. Rhoades,⁷³ F. Ricci,^{23,70} K. Riles,⁵⁹ N. A. Robertson,^{1,29} F. Robinet,³⁹ A. Rocchi,⁶¹ M. Rodruck,²⁸ L. Rolland,³ J. G. Rollins,¹ R. Romano,^{4,5} G. Romanov,¹¹² J. H. Romie,⁷ D. Rosińska,^{33,118} S. Rowan,²⁹ A. Rüdiger,⁹ P. Ruggi,²⁷ K. Ryan,²⁸ F. Salemi,⁹ L. Sammut,¹⁰³ V. Sandberg,²⁸ J. R. Sanders,⁵⁹ V. Sannibale,¹ I. Santiago-Prieto,²⁹ E. Saracco,⁴⁵ B. Sassolas,⁴⁵ B. S. Sathyaprakash,⁸ P. R. Saulson,¹⁵ R. Savage,²⁸ J. Scheuer,⁷⁶ R. Schilling,⁹ R. Schnabel,^{9,17} R. M. S. Schofield,⁵⁰ E. Schreiber,⁹ D. Schuette,⁹ B. F. Schutz,^{8,25} J. Scott,²⁹ S. M. Scott,⁶⁶ D. Sellers,⁷ A. S. Sengupta,¹¹⁹ D. Sentenac,²⁷ V. Sequino,^{61,69} A. Sergeev,⁹⁷ D. Shaddock,⁶⁶ S. Shah,^{42,10} M. S. Shahriar,⁷⁶ M. Shaltev,⁹ B. Shapiro,²⁰ P. Shawhan,⁵³ D. H. Shoemaker,¹¹ T. L. Sidery,²⁴ K. Siellez,⁴³ X. Siemens,¹⁶ D. Sigg,²⁸ D. Simakov,⁹ A. Singer,¹ L. Singer,¹ R. Singh,² A. M. Sintes,⁵⁵ B. J. J. Slagmolen,⁶⁶ J. Slutsky,⁹ J. R. Smith,²² M. Smith,¹ R. J. E. Smith,¹ N. D. Smith-Lefebvre,¹ E. J. Son,¹¹⁴ B. Sorazu,²⁹ T. Souradeep,¹³ L. Sperandio,^{61,69} A. Staley,³¹ J. Stebbins,²⁰ J. Steinlechner,⁹ S. Steinlechner,⁹ B. C. Stephens,¹⁶ S. Steplewski,⁴⁶ S. Stevenson,²⁴ R. Stone,⁷⁷ D. Stops,²⁴ K. A. Strain,²⁹ N. Straniero,⁴⁵ S. Strigin,³⁸ R. Sturani,^{120,48,49} A. L. Stuver,⁷ T. Z. Summerscales,¹²¹ S. Susmithan,⁴¹ P. J. Sutton,⁸ B. Swinkels,²⁷ M. Tacca,³⁰ D. Talukder,⁵⁰ D. B. Tanner,⁶ S. P. Tarabrin,⁹ R. Taylor,¹ A. P. M. ter Braack,¹⁰ M. P. Thirugnanasambandam,¹ M. Thomas,⁷ P. Thomas,²⁸ K. A. Thorne,⁷ K. S. Thorne,⁶⁴ E. Thrane,¹ V. Tiwari,⁶ K. V. Tokmakov,¹⁰⁶ C. Tomlinson,⁷⁹ A. Toncelli,^{18,32} M. Tonelli,^{18,32} O. Torre,^{18,19} C. V. Torres,⁷⁷ C. I. Torrie,^{1,29} F. Travasso,^{47,87} G. Traylor,⁷ M. Tse,^{31,11} D. Ugolini,¹²² C. S. Unnikrishnan,¹⁴ A. L. Urban,¹⁶ K. Urbanek,²⁰ H. Vahlbruch,¹⁷ G. Vajente,^{18,32} G. Valdes,⁷⁷ M. Vallisneri,⁶⁴ J. F. J. van den Brand,^{10,52} C. Van Den Broeck,¹⁰ S. van der Putten,¹⁰ M. V. van der Sluys,^{42,10} J. van Heijningen,¹⁰ A. A. van Veggel,²⁹ S. Vass,¹ M. Vasúth,⁸⁰ R. Vaulin,¹¹ A. Vecchio,²⁴ G. Vedovato,¹⁰⁴ J. Veitch,¹⁰ P. J. Veitch,⁹¹ K. Venkateswara,¹²³ D. Verkindt,³ S. S. Verma,⁴¹ F. Vetrano,^{48,49} A. Viceré,^{48,49} R. Vincent-Finley,¹¹¹ J.-Y. Vinet,⁴³ S. Vitale,¹¹ T. Vo,²⁸ H. Vocca,^{47,87} C. Vorvick,²⁸ W. D. Voudsen,²⁴ S. P. Vyachanin,³⁸ A. Wade,⁶⁶ L. Wade,¹⁶ M. Wade,¹⁶ M. Walker,² L. Wallace,¹ M. Wang,²⁴ X. Wang,⁵⁸ R. L. Ward,⁶⁶ M. Was,⁹ B. Weaver,²⁸ L.-W. Wei,⁴³ M. Weinert,⁹ A. J. Weinstein,¹ R. Weiss,¹¹ T. Welborn,⁷ L. Wen,⁴¹ P. Wessels,⁹ M. West,¹⁵ T. Westphal,⁹ K. Wette,⁹ J. T. Whelan,⁶⁰ D. J. White,⁷⁹ B. F. Whiting,⁶ K. Wiesner,⁹ C. Wilkinson,²⁸ K. Williams,¹¹¹ L. Williams,⁶ R. Williams,¹ T. Williams,¹²⁴ A. R. Williamson,⁸ J. L. Willis,¹²⁵ B. Willke,^{17,9} M. Wimmer,⁹ W. Winkler,⁹ C. C. Wipf,¹¹ A. G. Wiseman,¹⁶ H. Wittel,⁹ G. Woan,²⁹ J. Worden,²⁸ J. Yablon,⁷⁶ I. Yakushin,⁷ H. Yamamoto,¹ C. C. Yancey,⁵³ H. Yang,⁶⁴ Z. Yang,⁵⁸ S. Yoshida,¹²⁴ M. Yvert,³ A. Zadrożny,¹⁰¹ M. Zanolin,⁷³ J.-P. Zendri,¹⁰⁴ Fan Zhang,^{11,58} L. Zhang,¹ C. Zhao,⁴¹ X. J. Zhu,⁴¹ M. E. Zucker,¹¹ S. Zuraw,⁵⁴ and J. Zweizig¹

(LIGO Scientific Collaboration and Virgo Collaboration)

- ¹LIGO-California Institute of Technology, Pasadena, California 91125, USA
²Louisiana State University, Baton Rouge, Louisiana 70803, USA
³Laboratoire d'Annecy-le-Vieux de Physique des Particules (LAPP), Université de Savoie, CNRS/IN2P3, F-74941 Annecy-le-Vieux, France
⁴INFN, Sezione di Napoli, Complesso Universitario di Monte S. Angelo, I-80126 Napoli, Italy
⁵Università di Salerno, Fisciano, I-84084 Salerno, Italy
⁶University of Florida, Gainesville, Florida 32611, USA
⁷LIGO-Livingston Observatory, Livingston, Louisiana 70754, USA
⁸Cardiff University, Cardiff CF24 3AA, United Kingdom
⁹Albert-Einstein-Institut, Max-Planck-Institut für Gravitationsphysik, D-30167 Hannover, Germany
¹⁰Nikhef, Science Park, 1098 XG Amsterdam, The Netherlands
¹¹LIGO-Massachusetts Institute of Technology, Cambridge, Massachusetts 02139, USA
¹²Instituto Nacional de Pesquisas Espaciais, 12227-010 São José dos Campos, SP, Brazil
¹³Inter-University Centre for Astronomy and Astrophysics, Pune 411007, India
¹⁴Tata Institute for Fundamental Research, Mumbai 400005, India
¹⁵Syracuse University, Syracuse, New York 13244, USA
¹⁶University of Wisconsin–Milwaukee, Milwaukee, Wisconsin 53201, USA
¹⁷Leibniz Universität Hannover, D-30167 Hannover, Germany
¹⁸INFN, Sezione di Pisa, I-56127 Pisa, Italy
¹⁹Università di Siena, I-53100 Siena, Italy
²⁰Stanford University, Stanford, California 94305, USA
²¹The University of Mississippi, University, Mississippi 38677, USA
²²California State University Fullerton, Fullerton, California 92831, USA
²³INFN, Sezione di Roma, I-00185 Roma, Italy
²⁴University of Birmingham, Birmingham B15 2TT, United Kingdom
²⁵Albert-Einstein-Institut, Max-Planck-Institut für Gravitationsphysik, D-14476 Golm, Germany
²⁶Montana State University, Bozeman, Montana 59717, USA
²⁷European Gravitational Observatory (EGO), I-56021 Cascina, Pisa, Italy
²⁸LIGO-Hanford Observatory, Richland, Washington 99352, USA
²⁹SUPA, University of Glasgow, Glasgow G12 8QQ, United Kingdom
³⁰APC, AstroParticule et Cosmologie, Université Paris Diderot, CNRS/IN2P3, CEA/Irfu, Observatoire de Paris, Sorbonne Paris Cité, 10, rue Alice Domon et Léonie Duquet, F-75205 Paris Cedex 13, France
³¹Columbia University, New York, New York 10027, USA
³²Università di Pisa, I-56127 Pisa, Italy
³³CAMK-PAN, 00-716 Warsaw, Poland
³⁴Astronomical Observatory Warsaw University, 00-478 Warsaw, Poland
³⁵INFN, Sezione di Genova, I-16146 Genova, Italy
³⁶Università degli Studi di Genova, I-16146 Genova, Italy
³⁷San Jose State University, San Jose, California 95192, USA
³⁸Faculty of Physics, Lomonosov Moscow State University, Moscow 119991, Russia
³⁹LAL, Université Paris-Sud, IN2P3/CNRS, F-91898 Orsay, France
⁴⁰NASA/Goddard Space Flight Center, Greenbelt, Maryland 20771, USA
⁴¹University of Western Australia, Crawley, WA 6009, Australia
⁴²Department of Astrophysics/IMAPP, Radboud University Nijmegen, P.O. Box 9010, 6500 GL Nijmegen, The Netherlands
⁴³Université Nice-Sophia-Antipolis, CNRS, Observatoire de la Côte d'Azur, F-06304 Nice, France
⁴⁴Institut de Physique de Rennes, CNRS, Université de Rennes 1, F-35042 Rennes, France
⁴⁵Laboratoire des Matériaux Avancés (LMA), IN2P3/CNRS, Université de Lyon, F-69622 Villeurbanne, Lyon, France
⁴⁶Washington State University, Pullman, Washington 99164, USA
⁴⁷INFN, Sezione di Perugia, I-06123 Perugia, Italy
⁴⁸INFN, Sezione di Firenze, I-50019 Sesto Fiorentino, Firenze, Italy
⁴⁹Università degli Studi di Urbino "Carlo Bo," I-61029 Urbino, Italy
⁵⁰University of Oregon, Eugene, Oregon 97403, USA
⁵¹Laboratoire Kastler Brossel, ENS, CNRS, UPMC, Université Pierre et Marie Curie, F-75005 Paris, France
⁵²VU University Amsterdam, 1081 HV Amsterdam, The Netherlands
⁵³University of Maryland, College Park, Maryland 20742, USA
⁵⁴University of Massachusetts-Amherst, Amherst, Massachusetts 01003, USA
⁵⁵Universitat de les Illes Balears, E-07122 Palma de Mallorca, Spain

- ⁵⁶*Università di Napoli “Federico II,” Complesso Universitario di Monte S. Angelo, I-80126 Napoli, Italy*
- ⁵⁷*Canadian Institute for Theoretical Astrophysics, University of Toronto, Toronto, Ontario M5S 3H8, Canada*
- ⁵⁸*Tsinghua University, Beijing 100084, China*
- ⁵⁹*University of Michigan, Ann Arbor, Michigan 48109, USA*
- ⁶⁰*Rochester Institute of Technology, Rochester, New York 14623, USA*
- ⁶¹*INFN, Sezione di Roma Tor Vergata, I-00133 Roma, Italy*
- ⁶²*National Tsing Hua University, Hsinchu Taiwan 300*
- ⁶³*Charles Sturt University, Wagga Wagga, NSW 2678, Australia*
- ⁶⁴*Caltech-CaRT, Pasadena, California 91125, USA*
- ⁶⁵*Pusan National University, Busan 609-735, Korea*
- ⁶⁶*Australian National University, Canberra, ACT 0200, Australia*
- ⁶⁷*Carleton College, Northfield, Minnesota 55057, USA*
- ⁶⁸*INFN, Gran Sasso Science Institute, I-67100 L’Aquila, Italy*
- ⁶⁹*Università di Roma Tor Vergata, I-00133 Roma, Italy*
- ⁷⁰*Università di Roma “La Sapienza,” I-00185 Roma, Italy*
- ⁷¹*University of Brussels, Brussels 1050 Belgium*
- ⁷²*Sonoma State University, Rohnert Park, California 94928, USA*
- ⁷³*Embry-Riddle Aeronautical University, Prescott, Arizona 86301, USA*
- ⁷⁴*The George Washington University, Washington, DC 20052, USA*
- ⁷⁵*University of Cambridge, Cambridge CB2 1TN, United Kingdom*
- ⁷⁶*Northwestern University, Evanston, Illinois 60208, USA*
- ⁷⁷*The University of Texas at Brownsville, Brownsville, Texas 78520, USA*
- ⁷⁸*University of Minnesota, Minneapolis, Minnesota 55455, USA*
- ⁷⁹*The University of Sheffield, Sheffield S10 2TN, United Kingdom*
- ⁸⁰*Wigner RCP, RMKI, H-1121 Budapest, Konkoly Thege Miklósút 29-33, Hungary*
- ⁸¹*University of Sannio at Benevento, I-82100 Benevento, Italy*
- ⁸²*INFN, Gruppo Collegato di Trento, I-38050 Povo, Trento, Italy*
- ⁸³*Università di Trento, I-38050 Povo, Trento, Italy*
- ⁸⁴*Montclair State University, Montclair, New Jersey 07043, USA*
- ⁸⁵*The Pennsylvania State University, University Park, Pennsylvania 16802, USA*
- ⁸⁶*MTA Eötvös University, “Lendület” A. R. G., Budapest 1117, Hungary*
- ⁸⁷*Università di Perugia, I-06123 Perugia, Italy*
- ⁸⁸*Rutherford Appleton Laboratory, HSIC, Chilton, Didcot, Oxon OX11 0QX, United Kingdom*
- ⁸⁹*Perimeter Institute for Theoretical Physics, Ontario N2L 2Y5, Canada*
- ⁹⁰*American University, Washington, DC 20016, USA*
- ⁹¹*University of Adelaide, Adelaide, SA 5005, Australia*
- ⁹²*Raman Research Institute, Bangalore, Karnataka 560080, India*
- ⁹³*Korea Institute of Science and Technology Information, Daejeon 305-806, Korea*
- ⁹⁴*Białystok University, 15-424 Białystok, Poland*
- ⁹⁵*University of Southampton, Southampton SO17 1BJ, United Kingdom*
- ⁹⁶*IISER-TVM, CET Campus, Trivandrum Kerala 695016, India*
- ⁹⁷*Institute of Applied Physics, Nizhny Novgorod 603950, Russia*
- ⁹⁸*Seoul National University, Seoul 151-742, Korea*
- ⁹⁹*Hanyang University, Seoul 133-791, Korea*
- ¹⁰⁰*IM-PAN, 00-956 Warsaw, Poland*
- ¹⁰¹*NCBJ, 05-400 Świerk-Otwock, Poland*
- ¹⁰²*Institute for Plasma Research, Bhat, Gandhinagar 382428, India*
- ¹⁰³*The University of Melbourne, Parkville, VIC 3010, Australia*
- ¹⁰⁴*INFN, Sezione di Padova, I-35131 Padova, Italy*
- ¹⁰⁵*Monash University, Victoria 3800, Australia*
- ¹⁰⁶*SUPA, University of Strathclyde, Glasgow G1 1XQ, United Kingdom*
- ¹⁰⁷*ESPCI, CNRS, F-75005 Paris, France*
- ¹⁰⁸*Argentinian Gravitational Wave Group, Cordoba Cordoba 5000, Argentina*
- ¹⁰⁹*Università di Camerino, Dipartimento di Fisica, I-62032 Camerino, Italy*
- ¹¹⁰*The University of Texas at Austin, Austin, Texas 78712, USA*
- ¹¹¹*Southern University and A&M College, Baton Rouge, Louisiana 70813, USA*
- ¹¹²*College of William and Mary, Williamsburg, Virginia 23187, USA*
- ¹¹³*IISER-Kolkata, Mohanpur, West Bengal 741252, India*
- ¹¹⁴*National Institute for Mathematical Sciences, Daejeon 305-390, Korea*

¹¹⁵*Hobart and William Smith Colleges, Geneva, New York 14456, USA*¹¹⁶*RRCAT, Indore MP 452013, India*¹¹⁷*SUPA, University of the West of Scotland, Paisley PA1 2BE, United Kingdom*¹¹⁸*Institute of Astronomy, 65-265 Zielona Góra, Poland*¹¹⁹*Indian Institute of Technology, Gandhinagar Ahmedabad Gujarat 382424, India*¹²⁰*Instituto de Física Teórica, University Estadual Paulista/International Center for Theoretical Physics-South American Institute for Research, São Paulo SP 01140-070, Brazil*¹²¹*Andrews University, Berrien Springs, Michigan 49104, USA*¹²²*Trinity University, San Antonio, Texas 78212, USA*¹²³*University of Washington, Seattle, Washington 98195, USA*¹²⁴*Southeastern Louisiana University, Hammond, Louisiana 70402, USA*¹²⁵*Abilene Christian University, Abilene, Texas 79699, USA*

(Received 9 June 2014; published 15 September 2014)

We present the first results of an all-sky search for continuous gravitational waves from unknown spinning neutron stars in binary systems using LIGO and Virgo data. Using a specially developed analysis program, the TwoSpect algorithm, the search was carried out on data from the sixth LIGO science run and the second and third Virgo science runs. The search covers a range of frequencies from 20 Hz to 520 Hz, a range of orbital periods from 2 to $\sim 2,254$ h and a frequency- and period-dependent range of frequency modulation depths from 0.277 to 100 mHz. This corresponds to a range of projected semimajor axes of the orbit from $\sim 0.6 \times 10^{-3}$ ls to $\sim 6,500$ ls assuming the orbit of the binary is circular. While no plausible candidate gravitational wave events survive the pipeline, upper limits are set on the analyzed data. The most sensitive 95% confidence upper limit obtained on gravitational wave strain is 2.3×10^{-24} at 217 Hz, assuming the source waves are circularly polarized. Although this search has been optimized for circular binary orbits, the upper limits obtained remain valid for orbital eccentricities as large as 0.9. In addition, upper limits are placed on continuous gravitational wave emission from the low-mass x-ray binary Scorpius X-1 between 20 Hz and 57.25 Hz.

DOI: [10.1103/PhysRevD.90.062010](https://doi.org/10.1103/PhysRevD.90.062010)

PACS numbers: 95.30.Sf, 95.85.Sz, 04.30.Tv

I. INTRODUCTION

Rapidly rotating, nonaxisymmetric neutron stars are predicted to emit continuous, nearly monochromatic gravitational waves. Using data from previous Laser Interferometer Gravitational Wave Observatory (LIGO) [1] and Virgo [2] science runs, other all-sky searches have been carried out for continuous gravitational wave signals from isolated, spinning neutron stars. Past all-sky searches include two different searches on LIGO science run 2 (S2) data [3,4]; three StackSlide-like search algorithms [5,6] and the first Einstein@Home distributed computing search [7] on LIGO science run 4 (S4) data; and a PowerFlux search [8,9] and Einstein@Home search [10,11] carried out on LIGO science run 5 (S5) data. None of these searches directly addressed continuous waves from a neutron star in an unknown binary system, and none had appreciable sensitivity to such sources because of the orbital modulation effects discussed below. Previous searches have been carried out, however, for a signal from the known low-mass x-ray binary system, Scorpius X-1, where the binary orbital parameters are reasonably constrained. One method used LIGO S2 data [3], and a different method used LIGO S4 data [12] and S5

data [13]. This article presents an explicit search for continuous waves from unknown neutron stars in binary systems, as well as a directed search for gravitational waves from Scorpius X-1.

Although the waves emitted by a spinning neutron star are nearly monochromatic, a gravitational wave detector located on Earth would observe a frequency-modulated signal caused by the motion of Earth [14]. Additionally, if such a source is located in a binary system, then the observed waves will have a frequency modulation imposed by the motion of the source in the binary system [15,16]. Together, these frequency modulations make searches for unknown, spinning binary neutron stars emitting continuous gravitational waves computationally demanding.

Previous searches, not accounting for the orbital modulations, would have been much less sensitive to stars in binary systems with induced frequency modulation amplitudes much greater than the frequency spacing between search templates ($\sim 5\text{--}500$ μHz , depending on the search method). In addition, while a very large amplitude continuous gravitational wave source in a binary system could produce outliers in other searches, the follow-up of those outliers would have likely rejected them because they do not follow the expected frequency evolution of an isolated source of continuous gravitational waves. Regardless, the

* evan.goetz@aei.mpg.de

upper limits set by these searches would be unreliable for sources in binary systems with significant frequency modulation.

Explicitly including the effects due to unknown binary orbital parameters in the other all-sky StackSlide-like [4,6,8,9] or Einstein@Home [7,10,11] algorithms would be computationally prohibitive. Thus, new methods are required to perform such a search with limited computational resources [16,17]. These new techniques require some sacrifice of strain sensitivity to gravitational waves in order to significantly reduce the computational demands of such a search.

One such algorithm, called TwoSpect [16], has been developed and implemented, and a search has been carried out with it using recently collected LIGO and Virgo data. The TwoSpect algorithm relies on the periodic nature of the frequency modulation caused by the binary orbit. Spectrograms of gravitational wave detector data are created after correcting for the Earth's known rotation and orbital motion, and then Fourier transformations of each frequency bin of the barycentered spectrogram are computed. These successive Fourier transforms enable efficient detection of frequency modulated signals because the modulation has fixed periodicity. Although optimized for circular orbits, the methodology used to obtain upper limits on source strengths remains sensitive for eccentricities as large as 0.9.

This article is organized as follows: Sec. II discusses neutron stars in binary systems and the assumed signal model; Sec. III briefly describes the LIGO and Virgo gravitational wave detectors; Sec. IV discusses the TwoSpect method; Sec. V describes the analysis of the detector data, and Sec. VI gives the results of the analysis; Sec. VII summarizes the conclusions of this work.

II. ASTROPHYSICAL SOURCES

Spinning neutron stars in binary systems are attractive sources in searches for continuous gravitational waves because accretion from a companion may cause an asymmetrical quadrupole moment of inertia of the spinning neutron star. Many mechanisms have been proposed where gravitational wave emission continues after accretion of material has subsided. For instance, the magnetic field of the neutron star can guide the accretion flow to “hot spots” which could build up the neutron star ellipticity close to that allowed by the maximum breaking strain of the crust [18], with possibly sustained localized mass accumulation [19], depending on nuclear equation of state [20], material sinking [21], resistive relaxation [22] and magnetic bottling stability [23]. In addition, magnetic fields could create nonaxisymmetric deformations of the neutron star interior [24], or *r*-mode oscillations of the neutron star might be sustained, causing the star to emit gravitational waves [25,26].

Accreting neutron stars can be spun up by acquiring angular momentum from the infalling matter. All-sky surveys of millisecond pulsars have found that no neutron stars are spinning close to their predicted break-up frequency ($\nu \sim 1400$ Hz) [27]. Since the observed spin frequency range of actively accreting millisecond pulsars is $180 \text{ Hz} < \nu < 600 \text{ Hz}$ [28], there may be a competing mechanism preventing the spin-up of the neutron star from reaching the break-up frequency.

It has been postulated that there exists a torque balance between the accretion spin-up and the gravitational emission spin-down [18,29,30]. In such a case, those neutron stars accreting at the highest rates should have the highest gravitational wave emissions. Using this relation to balance spin-down of gravitational wave emission with x-ray luminosity (a measure of the accretion rate), the dimensionless gravitational wave amplitude, h_0 , is given by

$$h_0 = 2.7 \times 10^{-26} \left(\frac{f}{800 \text{ Hz}} \right)^{-1/2} \times \left(\frac{F_x}{3.9 \times 10^{-7} \text{ erg cm}^{-2} \text{ s}^{-1}} \right)^{1/2}, \quad (1)$$

where f is the gravitational wave frequency and F_x is the average bolometric x-ray flux detected at the Earth. The x-ray luminosity is scaled to the average bolometric flux of Scorpius X-1 (Sco X-1). If *r*-mode instabilities are driven by the accretion of material, then the gravitational wave amplitude could be increased as [31]

$$h_0 = 3.3 \times 10^{-26} \left(\frac{f}{800 \text{ Hz}} \right)^{-1/2} \times \left(\frac{F_x}{3.9 \times 10^{-7} \text{ erg cm}^{-2} \text{ s}^{-1}} \right)^{1/2}. \quad (2)$$

A. Gravitational wave signal model

The expected waveform of a nonaxisymmetric spinning neutron star observed by a gravitational wave interferometer is

$$h(t) = h_0 F_+(t, \alpha, \delta, \psi) \frac{1 + \cos^2(\iota)}{2} \cos[\Phi(t)] + h_0 F_\times(t, \alpha, \delta, \psi) \cos(\iota) \sin[\Phi(t)], \quad (3)$$

where F_+ and F_\times are the detector response functions (antenna patterns) to “plus” and “cross” polarized gravitational waves, α and δ are the right ascension and declination of a particular sky location, ψ is the polarization angle of the waves, ι is the inclination angle of the neutron star rotational axis to the line of sight, and $\Phi(t)$ is the phase evolution of the gravitational wave signal. The assumed instantaneous phase evolution is given by

$$\begin{aligned} \Phi(t) = & \Phi_0 + 2\pi f_0(t - t_{\text{ref}}) \\ & + 2\pi\Delta f_{\text{obs}} \sin[\Omega(t - t_{\text{asc}})]/\Omega, \end{aligned} \quad (4)$$

where t is the time in the Solar System barycenter (SSB) frame, Φ_0 and f_0 are phase and frequency, respectively, determined at reference time t_{ref} , and t_{asc} is a given time of the orbital ascending node. The observed frequency modulation depth Δf_{obs} and period of frequency modulation $P = 2\pi\Omega^{-1}$ are caused by the motion of the source.

We assume that any spin-down effects [$2\pi\dot{f}(t - t_0)^2$ and higher order terms] in the phase evolution of the source are negligible during the observation time and that the orbit is circular and nonrelativistic. Electromagnetic observational evidence has shown that pulsars in binary systems typically have very small spin-downs, $|\dot{\nu}| < 10^{-15} \text{ Hz s}^{-1}$ (although larger spin-down could imply larger-amplitude gravitational wave emission) and that they also have nearly circular orbits. It may be possible, however, that a neutron star in a binary system with a small spin-down value could be a strong emitter of gravitational radiation (for example, the neutron star is in torque balance equilibrium). Even though a circular orbit phase model has been assumed, the detection algorithm is sensitive to the more general case of an eccentric orbit.

The gravitational wave amplitude for a nonaxisymmetric spinning neutron star with $l = m = 2$ mass quadrupole moment is

$$h_0 = \frac{16\pi^2 G I \epsilon \nu^2}{c^4 d}, \quad (5)$$

where G is the gravitational constant, c is the speed of light in a vacuum, I is the principal moment of inertia with respect to the spin axis, ϵ is the equatorial ellipticity of the neutron star, ν is the rotational frequency of the neutron star, and d is the distance to the neutron star. A spinning neutron star will emit continuous gravitational waves with frequency $f_0 = 2\nu$.

The observed modulation depth is related to the maximum modulation depth, Δf_{max} , by

$$\Delta f_{\text{obs}} = \Delta f_{\text{max}} \sin i, \quad (6)$$

where i is the inclination angle of the binary orbital plane with respect to the vector that points from the detector to the sky position. Assuming a circular, nonrelativistic orbit, the maximum observable Doppler shift will occur for an edge-on observed system with the modulation depth given by [16]

$$\begin{aligned} \Delta f_{\text{max}} \approx & 1.82 \left(\frac{f_0}{1 \text{ kHz}} \right) \left(\frac{M_{\text{NS}}}{1.4 M_{\odot}} \right)^{1/3} \\ & \times \left(\frac{P}{2 \text{ h}} \right)^{-1/3} \left[\frac{q}{(1+q)^{2/3}} \right] \text{ Hz}, \end{aligned} \quad (7)$$

where M_{NS} is the mass of the neutron star and $q \equiv M_2/M_{\text{NS}}$ is the mass ratio of the companion mass to the neutron star mass.

Alternatively, the observed modulation depth for a circular, nonrelativistic orbit can be written with directly observable parameters

$$\Delta f_{\text{obs}} \approx 0.8727 \left(\frac{f_0}{1 \text{ kHz}} \right) \left(\frac{P}{2 \text{ h}} \right)^{-1} \left(\frac{a \sin i}{1 \text{ ls}} \right) \text{ Hz}, \quad (8)$$

where $a \sin i$ is the projected semimajor axis (the projected radius of the orbit since we are concerned with nearly circular orbits) in units of light seconds (ls). Given a wide range of realistic orbital parameters, Eq. (8) shows that one must search frequency modulation depths easily reaching 1 Hz or greater, to cover the full range of possible binary systems.

III. LIGO AND VIRGO DETECTORS

Data taken in 2009-2010 with the 4-km-long ‘‘enhanced’’ LIGO detectors [1] and the 3-km-long Virgo detector [2] were used in this analysis. The LIGO and Virgo detectors are both power-recycled Michelson interferometers with Fabry-Perot arm cavities.

Following S5, a number of upgrades were made to the ‘‘initial’’ LIGO 4-km-long interferometers (H1 in Hanford, Washington, and L1 in Livingston Parish, Louisiana). The most substantial upgrades are as follows: (1) the initial 10 W laser was upgraded to a new 35 W laser, (2) an ‘‘output mode cleaner’’ was installed at the output port of the interferometer, (3) the radio-frequency detection scheme (heterodyne) was changed to a DC detection scheme (homodyne), and (4) the detection opto-electronics were moved to an in-vacuum, actively stabilized optical table to reduce seismic motion affecting the read-out optics and electronics. These upgrades constituted the enhanced LIGO interferometers [32].

Following the first Virgo science run (VSR1), several upgrades were made to improve the sensitivity of the detector for the subsequent second and third science runs. The main enhancements to the detector included the following (1) upgrading to a new 25 W laser, (2) installation of a thermal compensation system to reduce thermal effects of laser power absorption in the main interferometer mirrors, (3) replacement of read-out and control electronics with lower-noise components, and (4) between the second and third science runs, new, monolithic, low-loss, fused silica suspensions installed on the main interferometer mirrors [33].

During the period of 7 July 2009 to 20 October 2010, the two enhanced LIGO 4-km interferometers, H1 and L1, had their sixth science run (S6), while the Virgo V1 interferometer had its second science run (VSR2) concurrently from 7 July 2009 to 8 January 2010 and its third science run (VSR3) from 11 August 2010 to 19 October 2010. The increased input laser power of the upgraded LIGO detectors decreased the noise above 200 Hz compared to S5 by a factor of ~ 2 , with more modest improvements below

200 Hz. The Virgo detector has a better sensitivity compared to the enhanced LIGO detectors below ~ 50 Hz but worse sensitivity at higher frequencies.

IV. TWOSPECT ALGORITHM

The details of the TwoSpect method have been described previously [16]. We briefly summarize the algorithm here. Short segments (30 min or less) of gravitational wave detector data are Fourier transformed (so-called short Fourier transforms, or SFTs) using the fastest Fourier transform in the West (FFTW) algorithm [34], and the power of each Fourier coefficient is computed. Next, each SFT is weighted according to the noise present in the SFT, and by the antenna pattern of the detector (the sensitivity) to a given sky location at the particular time that the SFT data were recorded. Time spectrograms of SFTs over a narrow frequency band (~ 1 Hz) are created such that the frequency shift caused by Earth's motion is removed by sliding each SFT by an appropriate amount for a specific sky location. Then, for each such spectrogram, the Fourier transform of each frequency bin's powers as a function of time is computed and, from these Fourier coefficients, the power spectra of the second Fourier transform are determined.

The TwoSpect search for gravitational waves is hierarchically organized into two stages. First, a non-template-based algorithm searches the doubly Fourier-transformed data for interesting regions of parameter space that exceed a specific threshold value. Second, the interesting regions of parameter space are subjected to template-based tests in order to confirm or reject specific outliers. Whether or not an outlier has been found, an upper limit on gravitational wave amplitude is placed at each sky location.

A. Data preparation

The S6 and VSR2/3 data sets, each defined here with a length $T_{\text{obs}} = 40551300$ s, are divided into segments of length $T_{\text{SFT}} = 1800$ s. Each sequential segment overlaps the preceding segment by 50%, and each of these segments of data is windowed using the Hann window function, to suppress signal leakage into other frequency bins, before the Fourier transform is computed. The windowed Fourier transform is defined as

$$\tilde{s}_k = \frac{\Delta t}{C} \sum_{j=0}^{M-1} w_j s_j e^{-2\pi i j k / M}, \quad (9)$$

where $k = 0, 1, 2, \dots, (M-1)$, $\Delta t = T_{\text{SFT}}/M$ is the sampling interval, the window function is $w_j = 0.5[1 - \cos(2\pi j/M)]$, and $C = (\sum_{j=0}^{M-1} w_j^2/M)^{1/2} = (3/8)^{1/2}$. Physical frequency $f_k = k/T_{\text{SFT}}$ corresponds to $0 \leq k \leq M/2$. The ‘‘power’’ in bin k of SFT n is taken to be

$$P_k^n = \frac{2|\tilde{s}_k^n|^2}{T_{\text{SFT}}}. \quad (10)$$

The SFTs are adjusted for the changing detector velocity with respect to a fixed sky location by shifting SFT bins to correct for this effect in the same manner as other StackSlide-like algorithms [5,6]. A sequence of n (shifted) SFT powers are weighted and normalized by

$$\tilde{p}_k^n = \frac{F_n^2(P_k^n - \langle P_k \rangle^n)}{(\langle P_k \rangle^n)^2} \left[\sum_{n'}^N \frac{F_{n'}^4}{(\langle P_k \rangle^{n'})^2} \right]^{-1}, \quad (11)$$

where angle brackets $\langle \rangle$ indicate the running mean value over the inner index—the frequency bins, k , to estimate the noise background—and, assuming a circularly polarized gravitational wave,

$$F^2(t, \alpha, \delta) = F_+^2(t, \alpha, \delta) + F_\times^2(t, \alpha, \delta). \quad (12)$$

The dependence on ψ has been omitted because F^2 has no ψ dependence for circular polarization. Hence, particular SFTs that have low noise or for which the detector is favorably oriented to a sky position are weighted more heavily than SFTs that have high noise or for which the detector is unfavorably oriented.

The running mean values of the noise background are calculated from the running median values [35] of the SFT powers. The running median is converted to a mean value (assuming the P_k^n values follow an exponential distribution) including a bias factor for this analysis of a running median of 101 bins [6]. The running mean values are an estimate of the smoothly varying detector noise background that avoids biases from sharp spectral features of the detector noise (lines) and potential signals.

The Fourier transform of Eq. (11) is then computed for each frequency bin k and normalized such that the expectation value of the second Fourier transform in the presence of noise is equal to 1. For frequency bin k , the power as a function of second Fourier transform frequency, f' , is written as

$$Z_k(f') = \frac{|\mathcal{F}[\tilde{p}_k^n]|^2}{\langle \lambda(f') \rangle}, \quad (13)$$

where \mathcal{F} denotes a Fourier transform and $\langle \lambda(f') \rangle$ is the mean of the background noise estimate of the second Fourier transform. The values of $\lambda(f')$ are determined by Monte Carlo simulation using the noise estimates established from the SFTs and assuming the noise in the SFTs is due to Gaussian noise alone. The distribution of $Z_k(f')$ values from a Gaussian-noise time series follows a χ^2 distribution with 2 degrees of freedom and a mean of 1.0 to a good approximation, as discussed in [16].

Note that in this analysis, $Z_k(f')$ is directly proportional to h^4 because the power spectrum of SFT powers (directly

proportional to h^2) has been computed. This means that detection statistics computed from Z_k values will be directly proportional to h^4 .

B. First-stage detection statistic

The all-sky search begins with an untemplated search algorithm, incoherent harmonic summing (IHS) [16], to identify regions of parameter space to be searched later using templates and to set upper limits. It is useful to define a quantity that measures power at multiple harmonics of a fundamental frequency, f' . For example, one can fold each $Z_k(f')$ an integer $j = 1 \dots S$ times to define for a single frequency bin, k , the following statistic:

$$\mathcal{V}_k = \max \left\{ \sum_{j=1}^S [Z_k(jf') - \lambda(jf')] \right\}. \quad (14)$$

If a periodic signal is present, then the IHS algorithm will accumulate signal power from the higher harmonic frequencies into the lower harmonic frequencies. The signal-to-noise ratios of the signal bins grow $\propto \sqrt{S}$, provided the sequence of harmonic powers have similar SNR in the original spectra. In practice, this increase in SNR is limited by the strength of the higher signal harmonics, giving the IHS technique a practical limit of $S \sim 5$ in this application.

To accumulate additional signal power, folded Z_k values are summed across sequential values of k according to

$$\mathcal{W}(k_0, f', \Delta k) = \sum_{k=k_0-\Delta k}^{k_0+\Delta k} \sum_{j=1}^S [Z_k(jf') - \lambda(jf')], \quad (15)$$

before determining the maximum value. Computing $\mathcal{W}(k_0, f', \Delta k)$ “compresses” the second Fourier transformed data. Then, for a chosen Δk , the maximum value of $\mathcal{W}(k_0, f')$ is determined. As described in Sec. IV A, the values of \mathcal{W} are proportional to h^4 .

At the end of the first stage, any IHS statistic passing a threshold of a predetermined false alarm probability is passed to the second, template-based stage for more stringent follow-up tests using test values of f (derived from k_0), P (derived from f'), and Δf_{obs} (derived from Δk). Whether or not any candidates are found in the first stage, a frequentist 95% confidence upper limit is placed based on the highest statistic found in the first stage (see Sec. IV E).

C. Second-stage detection statistic

The second stage of the pipeline tests candidate outliers from the first stage against templates that are based on putative signal patterns and weights in the second Fourier transform. Assume that the strain power for a putative signal is distributed among M pixels of the second Fourier transform for a narrow band of SFT frequencies, with the

fraction of the signal power in pixel m_i equal to $w(m_i)$. A useful statistic to sum pixel powers is

$$R = \frac{\sum_{i=0}^{M-1} w(m_i)[Z(m_i) - \lambda(m_i)]}{\sum_{i=0}^{M-1} [w(m_i)]^2}, \quad (16)$$

where $Z(m_i)$ is the second Fourier transform power in pixel m_i (each m_i is a unique value of k and f'), $\lambda(m_i)$ is the expected noise value of pixel m_i of the second Fourier transform, and the weights are normalized such that

$$\sum_{i=0}^{M-1} w(m_i) = 1, \quad (17)$$

where N is the total number of pixels in the region of interest of the second Fourier transform. In practice, due to computational constraints, the value of M in Eq. (16) is fixed to be no larger than 500. This limit is raised in follow-up studies of particularly interesting candidates.

The weights are sorted such that $w(m_0)$ contains the greatest weight and $w(m_{M-1})$ contains the smallest weight. The weights $w(m_i)$ are determined by using a set of templates with parameters $(f, P, \Delta f)$ using the same T_{SFT} and T_{obs} as the search [16]. If the input time series of data is Gaussian, white noise, then the value of R is a weighted χ^2 variable with up to $2M$ degrees of freedom but shifted to have zero mean. Again, the second stage statistic R is proportional to h^4 .

For each candidate passed to the second stage, a number of different templates are tested using the “Gaussian” template approximation [16] with orbital period values up to the fifth harmonic or subharmonic from the originally identified orbital period value, as well as fractional orbital period values of $2/3$, $3/4$, $4/5$, $3/2$, $4/3$, and $5/4$ from the originally identified orbital period value (we refer to this misidentification as “harmonic confusion”). From the tested templates, only the most significant candidate (see Sec. IV D) is kept and followed up by searching a small region of $(f, P, \Delta f)$ with both Gaussian templates and with more exact templates. These template tests provide more stringent requirements for rejecting noise outliers.

D. Significance of outliers

To quantify the significance of a specific value of R_0 , given a set of $w(m_i)$, $Z(m_i)$, and an estimate of $\lambda(m_i)$, the false alarm probability $P(R \geq R_0)$ is computed. The false alarm probability is solved using the method described in [16] applying the formulas of [36]. The value computed for the false alarm probability assumes the underlying noise for each pixel is χ^2 distributed with 2 degrees of freedom with mean values given by $\lambda(m_i)$. The computed false alarm probability value does not take into account testing multiple points in parameter space. Section VI B describes how the significance is used in the follow-up analysis of outliers.

E. Determination of upper limits

At each sky location, the algorithm sets a frequentist 95% confidence level upper limit based on the highest calculated IHS statistic value in the searched frequency band, over the range of orbital periods and modulation depths. Upper limits are placed at this stage using the IHS because obtaining more sensitive template-based upper limits is computationally infeasible with available resources. Only promising outliers are followed up for detection using a templated search. Even in the event of a successful detection, however, IHS upper limits remain valid (see Figs. 5 and 6). In the presence of pure Gaussian noise, the IHS statistic is a χ^2 variable with $2AS$ degrees of freedom, where A is the number of SFT frequency bins summed, and S is the number of harmonics summed in the IHS algorithm. We wish to determine the amount of signal required such that the new IHS statistic value would exceed the highest found IHS statistic value 95% of the time.

To find the amount of signal required, we invert the noncentral χ^2 cumulative distribution function (CDF) so that the appropriate noncentrality parameter p is found such that only 5% of the distribution lies below the highest outlier value. The inversion is done using Newton's method. From the calculated value of p and the expected noise background, the value is converted to a value of h_0 such that, 95% of the time, the calculated value of h_0 is larger than any potentially present continuous gravitational wave signal in the data that has parameters within the parameter space searched by TwoSpect (see, e.g., Sec. V). The conversion factor is a simple scaling factor that relates the value of $p^{1/4}$ (recall that \mathcal{W} is proportional to h^4) to the 95% confidence level strain amplitude upper limit, $h_0^{95\%}$. The scaling factor is determined using injections of a wide variety of waveforms covering the parameter space searched. The all-sky upper limit in a given frequency band is then determined by selecting the largest value of $h_0^{95\%}$ from the entire set of sky coordinates searched for that frequency band.

This method of setting upper limits has been validated with simulated software injections and provides reliable results in bands that pass the data quality requirements described in Sec. VA.

V. ANALYSIS OF THE DATA

Data from the H1 and L1 detectors' sixth science run (S6) and V1 detector's second and third science runs (VSR2 and VSR3, collectively VSR2/3) were analyzed using the TwoSpect algorithm. Each detector's data set was analyzed separately with $T_{\text{obs}} = 40551300$ s. An outlier from one detector is required to be coincident in parameter space with an outlier in a second detector in order to be considered a candidate signal. Figure 1 shows the period-modulation depth parameter space values covered in this analysis using TwoSpect.

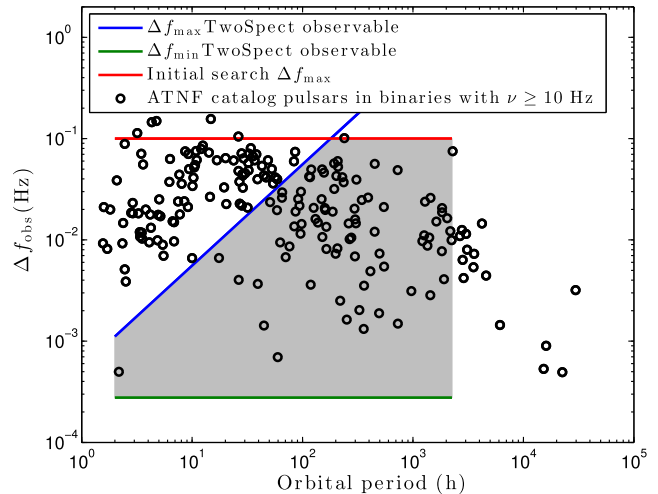


FIG. 1 (color online). Nominal parameter space that is analyzed using the TwoSpect algorithm (shaded region). The bounding curves given by Δf_{max} and Δf_{min} are limitations of the analysis, while the initial search boundary of $\Delta f_{\text{max}} = 0.1$ Hz is a choice. Data marked by circles are ATNF catalog pulsars found in binary systems with rotation frequencies ≥ 10 Hz [using Eq. (8) and assuming $f_0 = 2\nu$].

It is assumed that the sinusoidal term in Eq. (4) is constant during a single coherent observation interval; that is, the sinusoidal term is slowly evolving compared to the f_0 term. The signal is, therefore, assumed to be contained within one frequency bin for each coherent observation interval. This approximation restricts the orbital parameter space that can be observed: the longer a coherent observation, the more restricted the parameter space [16]. Longer coherent observation intervals, however, correspond to increased sensitivity to continuous wave signals. A trade-off is thus made in the sensitivity versus parameter space volume to be probed when conducting such a search.

LIGO S6 data from H1 and L1 were analyzed from 50 Hz to 520 Hz, covering a range of periods from 2 h to 2,254.4 h and modulation depths of 0.277 mHz to 100 mHz. Virgo VSR2/3 data were analyzed from 20 Hz to 100 Hz, over the same range of periods and modulation depths. The range of orbital periods has a lower limit determined by the coherence length of the SFTs, and an upper bound by requiring at least five orbits during the total observation time. The lower limit of modulation depths is determined by the coherence length of the SFTs, and the upper bound is chosen by covering a large region of parameter space without dramatically increasing computational costs. VSR2/3 data are only comparable to or better than LIGO S6 data in the aforementioned range of frequencies. Analyzing higher frequencies in the Virgo data would add to the total computing cost and add negligibly to the search sensitivity.

The TwoSpect program is part of the LIGO Analysis Library suite (LALSuite) software package [37]. TwoSpect

is written in C and is compiled against the LSC Algorithm Library (LAL), GNU Scientific Library (GSL) [38], and FFTW libraries. On the LIGO computer clusters, the analysis is divided into parallel “jobs” that are run on many computers simultaneously. Each job is an instance of the TwoSpect program and analyzes a 0.25 Hz frequency band and a small sky region (typically 200 sky grid locations).

A. Data quality validation

Ideally, the noise from a gravitational wave interferometer would be stationary Gaussian noise (in addition to any gravitational wave signal). In practice, data from the LIGO and Virgo detectors are generally stationary and nearly Gaussian on the time scale that one SFT is computed. There are occasions, however, when data must be excluded because of the following: (1) it is known that the interferometer data are corrupted (data quality flags are applied); (2) the segment of data passes data quality flags, but the data segment is non-Gaussian (a Kolmogorov-Smirnov test and/or Kuiper’s test fails); or (3) sharp, stationary spectral features prevent a full analysis of the selected frequency band. Examples of sharp, stationary spectral features include the following: power-line harmonics (50/60 Hz), mirror suspension violin modes, and calibration lines injected into the detector by actuating one of the end mirrors. Additionally, the detectors do not operate continuously during their science runs. There are periods of downtime, or other gaps in the detector data. We describe below the techniques used to select the data to be analyzed.

1. Science mode and data quality flags

Periods of time when the detector was operating in the nominal “science mode” are first selected. Next, a series of quality checks of the data—known as “data quality flags”—are applied to remove times when the detector data are known to be of poor quality. Examples include when the calibration of the detector is known to be outside a tolerance range, or when there were periods of very high wind speeds (see Table I) [39,40].

After these checks are applied, SFTs are created. The S6 data set contains 18,435 H1 and 16,429 L1 50% overlapping Hann-windowed SFTs with start times occurring an integer factor of $T_{\text{SFT}}/2$ from the start time of the first SFT. The resulting duty factors are 0.409 and 0.364 for H1

and L1, respectively. The VSR2/3 data set contains 17,879 50% overlapping Hann-windowed SFTs, corresponding to a duty factor of 0.733. SFTs consisting entirely of zeros fill in the excluded times not covered by these SFTs. The actual fraction of T_{obs} covered by the SFTs is somewhat different. Since S6 has only a slightly longer time baseline than T_{obs} , the duty factor is nearly identical. For VSR2/3, there is a long gap in between the science runs that results in a large reduction in the fraction of T_{obs} covered by the SFTs compared to the coverage of VSR2/3 science run time (see Table I).

2. Kolmogorov-Smirnov test and Kuiper’s test

After the SFTs are produced, each SFT is analyzed to determine whether the distribution of the powers follows that of an expected exponential distribution. Two useful tests are the Kolmogorov-Smirnov (KS) test and Kuiper’s test [41]. Those SFTs which do not pass these tests are removed from the analysis, and are replaced with SFTs consisting entirely of zeros. The threshold value for each of the KS and Kuiper’s tests is determined from the significance level on the null hypothesis of 0.05. With this threshold, SFTs are not rejected even if they contain potential signals with the expected gravitational wave signal amplitude. For certain 0.25 Hz frequency bands for an interferometer where data coverage is less than 10% of the total observation time due to disturbed, non-Gaussian data, no upper limits are placed in those frequency bands (see again Table I).

3. Line detection and flagging

Narrow spectral artifacts of terrestrial origin—also called “lines”—can potentially interfere with detection of gravitational wave signals. These disturbances are avoided by identifying potentially interfering lines (see below) and producing no further analysis of candidate signals that have interference caused by the disturbance. Upper limits are still placed, however, in frequency bands containing lines, although when the line fraction of a band exceeds 10% of the total band, no upper limit is placed, as the noise background estimate would be untrustworthy. This problem occurs primarily in the 50 to 200 Hz region of the enhanced LIGO detectors.

Sharp spectral features are identified as an excess of power over long time scales compared to the neighboring

TABLE I. Data usage in the S6 and VSR2/3 science runs.

Duty factor condition	H1	L1	V1
Interferometer in science mode with data quality flags during the science run(s)	0.506	0.463	0.778
Interferometer in science mode with data quality flags covered by SFTs	0.409	0.364	0.733
Fraction of $T_{\text{obs}} = 40551300$ s covered by SFTs	0.409	0.365	0.397
Median fraction of T_{obs} after KS and Kuiper’s tests in each 0.25 Hz band	0.383	0.316	0.366

frequency bins. The root-mean-square (RMS) power is computed for each noise-weighted SFT frequency bin as a function of time (without shifting the SFTs to account for detector motion). A running median of these RMS values is computed over the band of interest and is used to normalize the RMS values. Any normalized RMS value that exceeds an empirically determined threshold of 1.5 is flagged as a line.

4. Sidereal and daily modulations

Specific orbital period frequencies corresponding to the sidereal (86164.0905 s) and daily (86400.0 s) periods and up to the third harmonic are specifically avoided in this analysis, within a tolerance of ± 1 second FFT frequency bin for each harmonic. These frequencies can correspond to spurious artifacts in the analysis, and therefore no candidates are analyzed and no upper limits are placed at these putative binary orbital period values.

VI. RESULTS

The TwoSpect program produces two outputs: upper limit values and a list of outliers passing threshold tests over the parameter space searched. See Secs. [VIA](#) and [VIB](#), respectively, for more details.

A. All-sky upper limit results

Upper limits are established for each interferometer separately, with a single value at each sky location. The upper limit value for a given sky location is maximized over the $(f, P, \Delta f)$ parameter space range searched. The highest upper limit value over the entire sky for a given frequency band is then selected as the overall upper limit for that frequency band in a particular interferometer. Where there is more than one detector providing an upper limit in a given frequency band, the lowest of the upper limits is taken as the overall, combined upper limit value (see Fig. 2).

The values placed on upper limits of gravitational wave amplitude with 95% confidence assume the best-case scenario that the unobserved gravitational waves are circularly polarized. The true astrophysical population of gravitational wave sources is expected, however, to be uniformly distributed in orientation so that the polarization of the source waves can vary over a range of values covering completely circularly polarized waves, to completely linearly polarized waves. In the latter case, a multiplicative scale factor of ≈ 3.3 should be applied to the results shown in Fig. 2. In the case of random pulsar orientations, however, a scale factor of ≈ 2.6 is applied to the circular polarization results as shown in Fig. 2. Additionally, these upper limits are valid only if the source has a spin-down value $|\dot{f}| \leq 1 \times 10^{-10}$ Hz/s.

If the source is in an eccentric orbit with its companion, then the assumed phase evolution can be a poor

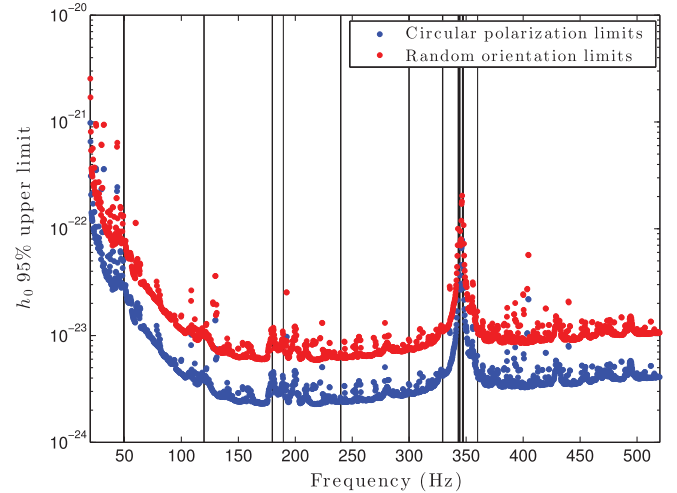


FIG. 2 (color). All-sky strain upper limit results of S6/VSR2-3 for continuous gravitational waves assuming the source waves are circularly polarized (blue points) or randomly polarized from randomly oriented sources (red points). The vertical black lines indicate 0.25 Hz frequency bands in which no upper limits have been placed. The smoothness of the curve is interrupted due to various instrumental artifacts, such as the violin resonances of the mirror suspensions near 350 Hz.

approximation to the true phase evolution of the source. However, whether an orbit is circular or eccentric, the modulated signal will spend more time in certain frequency bins within the modulation band (generating a stronger signal at those frequencies) and traverse other bins more rapidly (generating a weaker signal). The IHS statistic is relatively insensitive to the details of the shape of the modulation, responding only to its periodic structure in the second Fourier transform. Upper limits are still valid in this case, even for orbital eccentricities up to 0.9. An outlier caused by a gravitational wave source in an eccentric orbit may have poorly reconstructed signal parameters compared to the true source parameters.

The upper limits presented above assume that a putative signal could take any parameter values in the ranges searched. Suppose there are many different signals contained in the data, all of them having the same h_0 value but with Δf_{obs} values that could possibly range from 0.277 mHz to 100 mHz. In this case, the value of \mathcal{W} from Eq. (15) is diminished for higher values of Δf_{obs} . This results in upper limits that are dominated by those putative signals having large Δf_{obs} . One can show empirically that the upper limit values improve (smaller strain upper limits) as $(\Delta f_{\text{obs}})^{0.4}$ for smaller cutoffs in Δf_{obs} .

B. All-sky outlier follow-up results

Outliers reported from the first stage of the pipeline, the IHS algorithm, are tested using the second stage in order to confirm or reject each candidate. Those outliers passing the second, template-based stage are ranked by their false

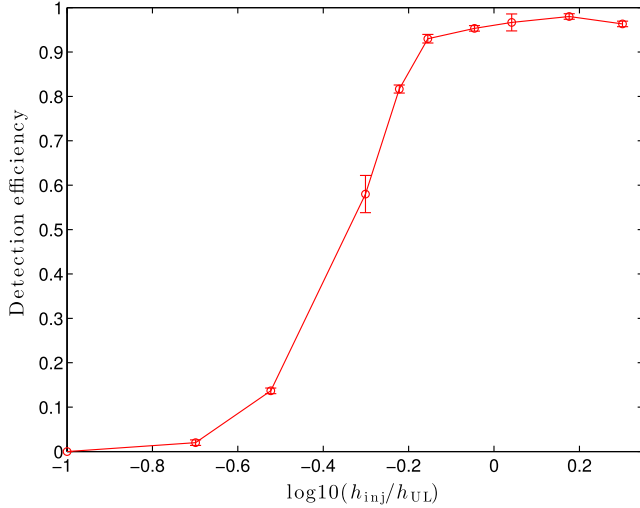


FIG. 3 (color online). The efficiency of signals passing the given coincidence requirements as a function of the injection amplitude (normalized to the upper limit value at the specific frequency of the injection).

alarm probability value, which indicates their significance of occurring in Gaussian noise alone. The false alarm probability of a weighted sum of χ^2 variables is numerically determined using methods described in [16,36]. Only outliers whose false alarm probability in a single detector is more significant than 10^{-18} , corresponding to a Gaussian SNR of ~ 8.8 , are followed up on as possible candidate gravitational wave signals. Such a strict threshold is set in order to reduce the number of outliers produced by non-Gaussian noise artifacts.

Those candidates from each detector with a fiducial signal frequency greater than 50 Hz are then subjected to multidetector coincidence tests in the multidimensional search parameter space. Coincidence requirements were tested using simulated signals to determine the false dismissal probability as a function of the injected strain values (see Fig. 3). The choice of coincidence requirements (see Table II) are shown to be sensible given that the false dismissal probability is, on average, no greater than 5% at the upper limit value (see Fig. 3). Coincident candidates are required to have an orbital period difference dP that scales with period and modulation depth as

TABLE II. Coincidence requirements for follow-up of outliers between two detectors.

Parameter	Allowed difference
Gravitational wave frequency mismatch	0.556 mHz
Orbital period mismatch ^a	See Eq. (18)
Modulation depth mismatch	0.556 mHz
Sky position mismatch	$0.1(800 \text{ Hz}/f)$ rad

^aOutliers may have an improperly identified orbital period due to harmonic confusion. Three higher harmonics and three subharmonics are tested in addition to the fiducial orbital period.

$$dP < (4.5T_{\text{obs}})^{-1} \times \min[P_1^2(\Delta f_1/3.6 \text{ mHz})^{-1/2}, P_2^2(\Delta f_2/3.6 \text{ mHz})^{-1/2}], \quad (18)$$

where P_1 and P_2 are the two identified orbital period values and Δf_1 and Δf_2 are the two identified modulation depths of the outliers in each detector. The coincidence requirements also allow for harmonic confusion in P_1 or P_2 up to the third harmonic or subharmonic.

The observed loss in detection efficiency is the result of restricting the first stage of the pipeline to pass only the five most interesting outliers to the second stage of the pipeline in order to limit computational resources spent in the second stage. The limitation means that the five outliers can sometimes ($\sim 5\%$ of the time) have correlated offsets in their parameters from the true waveform parameters (for example, offset from the fiducial frequency and modulation depth by a correlated amount), but the second stage is unable to find the true parameters from this limited subset of outliers simultaneously in two or more detectors. On average, the false dismissal of a simulated, large amplitude signal is $\sim 5\%$. Considering those simulations where a simulated signal with modulation depth Δf is close to the maximum observable modulation depth using TwoSpect ($\Delta f/\Delta f_{\text{max}} \gtrsim 0.3$; see Fig. 1), the false dismissal probability increases above 5%, approaching 50% false dismissal at the highest values of Δf . On the other hand, the false dismissal probability falls below 5% when the ratio $\Delta f/\Delta f_{\text{max}}$ becomes small ($\lesssim 0.1$). The false dismissal probability of the outlier follow-up analysis, however, does not affect the ability of the TwoSpect pipeline to set accurate upper limits on h_0 .

Pairwise combinations are made in each detector where for each outlier of the first detector only the most significant outlier of the second detector passing the coincidence requirements is retained. The same procedure is performed with the detector lists reversed. From this final list of outliers passing coincidence requirements, the outliers are grouped into narrow frequency bands (typically less than ~ 30 mHz) for further, manual inspection. The pairwise combination that has the smallest false alarm probability is considered representative of the outliers in each group [42]. The sky position of the pair is then averaged and given in Table III.

All of the outliers listed in Table III are found to be associated with known detector artifacts [39,40]. Most of the outliers are caused by a comb of 1 Hz, 2 Hz, or 16 Hz harmonics associated with the LIGO data acquisition system (DAQ). Another outlier is also due to a 392.2 Hz DAQ line. Two of the outliers are due to fake continuous gravitational wave signals with unrealistically large amplitudes injected into the detectors by modulating the interferometer arm lengths (see, e.g., Ref. [11] for additional details). Another outlier is due to a photon calibrator [43] calibration line at 404.7 Hz observed in the gravitational wave data channel. One other outlier is caused by a narrow,

TABLE III. Most significant outliers passing coincidence requirements grouped by frequency.

f_1 (Hz)	f_2 (Hz)	P_1 (ks)	P_2 (ks)	$\Delta f_{\text{obs},1}$ (mHz)	$\Delta f_{\text{obs},2}$ (mHz)	α (rad)	δ (rad)	Pair	Cause
61.000000	60.999735	7896.759938	7896.662780	100.000	99.722	4.6694	-1.5057	H1, V1	61 Hz line
90.010000	90.010130	6303.365336	7383.886742	3.333	3.611	6.0104	0.7223	H1, V1	90 Hz line
99.993333	99.993120	5406.840000	6337.503156	2.222	2.500	2.9800	-1.0808	H1, V1	100 Hz line, power line
108.856944	108.856944	86.166079	86.189136	0.278	0.556	3.1399	-0.5979	H1, L1	Fake pulsar 3
127.985321	127.985331	6190.885362	6180.988184	1.944	1.944	3.3945	0.0542	H1, L1	128 Hz line
134.092913	134.093056	7241.303571	803.807379	0.833	0.556	4.1811	0.7177	H1, L1	134.1 Hz line
192.498889	192.498889	8034.622934	7962.429248	94.444	93.889	2.3034	0.4624	H1, L1	Fake pulsar 8
217.997855	217.998056	6418.038156	5406.840000	2.222	2.500	4.7035	1.2218	H1, L1	218 Hz line
222.009771	222.010278	6208.893015	6337.503156	2.222	2.500	5.8797	1.2601	H1, L1	222 Hz line
249.999167	249.999444	7704.013336	6268.095166	4.167	4.444	1.0903	-1.3752	H1, L1	250 Hz line
256.027734	256.027500	6181.988411	5406.840000	2.222	2.500	6.2214	0.0942	H1, L1	256 Hz line
282.000000	282.000070	5497.564390	7526.367421	12.222	12.500	3.2944	-1.4169	H1, L1	282 Hz line
392.000139	392.000556	6424.556015	7546.515502	1.389	1.111	4.7405	1.2000	H1, L1	392 Hz line
392.179468	392.179958	6179.525429	6144.240561	2.222	1.667	4.1648	-1.4600	H1, L1	392.2 Hz DAQ line
404.750625	404.750140	6187.506004	6187.506004	60.278	60.278	4.9828	1.4683	H1, L1	404.7 Hz PCal line
410.000711	410.000278	7476.196898	7358.175495	24.722	24.167	0.3311	1.1811	H1, L1	410 Hz line
413.000000	412.999583	7240.033559	7462.679595	80.000	80.000	0.8309	-0.7947	H1, L1	413 Hz line

previously unidentified spectral artifact in H1 at 134.1 Hz coinciding with noise fluctuations in L1 to produce a candidate signal. Further studies of this outlier have shown that the signal characteristics are inconsistent with a gravitational wave signal. There are no TwoSpect outliers passing coincidence requirements in all of H1, L1, and V1 in the 50 to 100 Hz frequency band.

C. Upper limits on Scorpius X-1 emission

A separate, opportunistic analysis has been carried out for possible continuous gravitational wave emission from Sco X-1 using the same analysis as the all-sky search. In this second analysis, however, only the sky location of Sco X-1 was searched, and the parameter space was restricted to coincide with the projected semimajor axis $a \sin i = 1.44 \pm 0.18$ ls [44] and $P = 68023.70 \pm 0.0432$ s [45]. The highest frequency that can be searched, given these parameters and assuming the gravitational wave signal is contained within a single SFT frequency bin, is given by [16]

$$f \leq 78.9229 \left(\frac{P}{68023.70 \text{ s}} \right)^2 \times \left(\frac{a \sin i}{1.44 \text{ ls}} \right)^{-1} \left(\frac{T_{\text{SFT}}}{1800 \text{ s}} \right)^{-2} \text{ Hz.} \quad (19)$$

Assuming a worst-case scenario of $a \sin i = 1.44 + 3 \times 0.18 = 1.98$ ls and $T_{\text{SFT}} = 1800$ s, this relation limits the highest frequency that can be searched to be 57.25 Hz because we analyze only full-0.25 Hz frequency bands. Note that there is good reason, however, to believe that the Scorpius X-1 signal frequency would be higher than this value [46]. Using Eq. (8), the range of Δf_{obs} is frequency

dependent and ranges from 1.663 mHz to 10.470 mHz. Data from S6 were analyzed from 50 Hz up to 57.25 Hz, while VSR2/3 data were analyzed from 20 Hz up to 57.25 Hz.

The combined upper limits of the three interferometers are shown in Fig. 4. The upper limit results are typically about a factor of 3 better than the all-sky upper limits in this frequency range because only a single sky location needs to be searched, the range of orbital parameters to be searched is much smaller, and the incoherent harmonic summing

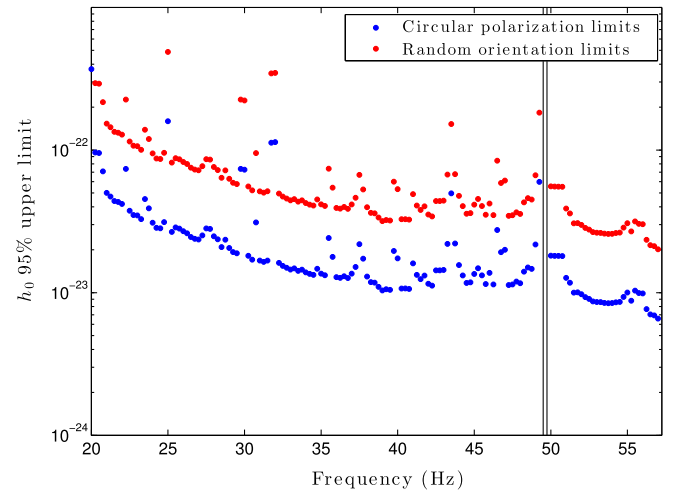


FIG. 4 (color online). Sco X-1 strain upper limit results of S6/VSR2-3 for continuous gravitational waves assuming the source waves are circularly polarized (lower points) or the source waves are randomly polarized with random pulsar orientations (upper points). The black vertical lines indicate 0.25 Hz frequency bands in which no upper limits have been placed.

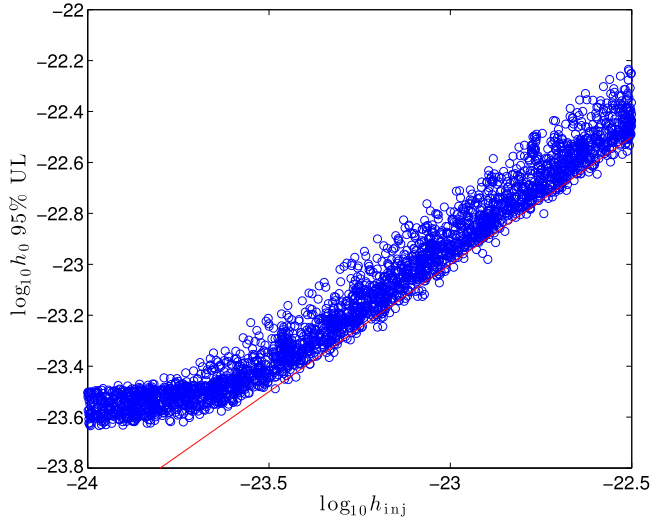


FIG. 5 (color online). Results from an upper limit validation test at 401 Hz, for circularly polarized waves. Each data point (blue circles) gives the 95% confidence upper limit set by TwoSpect for a given amplitude of a circularly polarized injection. The red line indicates a slope of 1. The upper limit procedure is valid provided that no more than 5% of the blue circle data points lie below the red line for any value of the injected amplitude.

step used $S = 10$ folds of the second FFT spectra as opposed to $S = 5$ for the all-sky search. These results are comparable to results from the fifth LIGO science run [13] using a different analysis technique [12].

A more sensitive search and more constraining upper limits could be obtained by optimizing the search pipeline

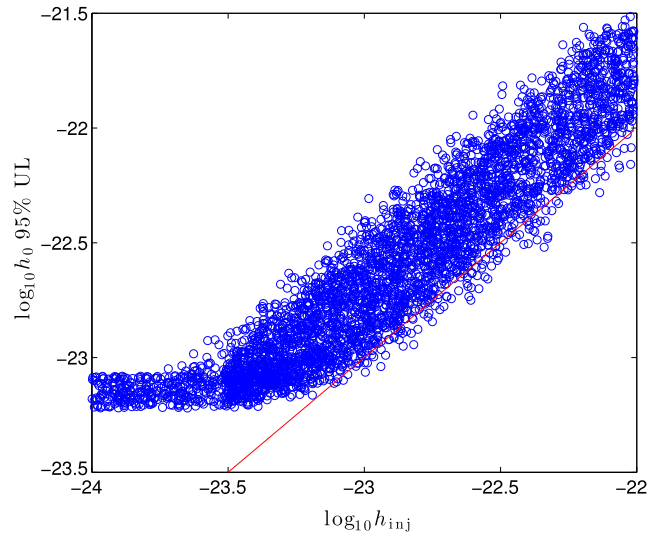


FIG. 6 (color online). Results from an upper limit validation test at 401 Hz, for randomly polarized waves. Each data point (blue circles) gives the 95% confidence upper limit set by TwoSpect for a given amplitude of a randomly polarized injection. The red line indicates a slope of 1. The upper limit procedure is valid provided that no more than 5% of the blue circle data points lie below the red line for any value of the injected amplitude.

for sources with known orbital parameters and unknown spin parameters. A future publication will detail these changes and demonstrate the improvement for such a search.

The methodology used in obtaining both the all-sky and Sco X-1 upper limits on source strain has been validated with simulated signal injections. Figures 5 and 6 illustrate validation tests for circularly and randomly polarized signals, and Fig. 3 shows derived detection efficiency.

VII. CONCLUSIONS

We have carried out the first explicit all-sky search for continuous gravitational wave signals from unknown spinning neutron stars in binary systems. This search was made possible through the use of the TwoSpect algorithm [16] to look for these sources. The search relies on the periodic modulation of the gravitational waves caused by the orbital motion of the source. The doubly Fourier-transformed data are processed by a hierarchical pipeline, subjecting the data to an incoherent harmonic summing stage, followed by comparing interesting regions of the data to templates that approximate the expected signal power in the doubly Fourier-transformed data.

This search has covered a broad range of possible gravitational wave frequencies—from 20 Hz to 520 Hz—binary orbital periods—from 2 h to 2,254.4 h—and frequency modulations—from 0.277 mHz to 100 mHz. These parameters cover a wide range of binary orbital parameters, and many known binary systems with neutron stars fall into the parameter space of this search. No plausible candidate continuous gravitational wave signal was observed. Upper limits are placed on continuous gravitational waves from unknown neutron stars in binary systems over the parameter space searched. The search carried out here is the most sensitive that covers such a wide range of the binary orbital parameter space [16].

Additionally, we have carried out a search for continuous gravitational waves from Sco X-1 between 20 Hz and 57.25 Hz. This search has covered only a small range of possible spin frequencies of Sco X-1 because of the limitations from using 1800 s SFTs. To more fully cover the range of possible Sco X-1 spin frequencies, future searches will need to use shorter coherent length SFTs. No outliers passed the same thresholds used for the all-sky search. Upper limits are placed on gravitational wave emission from Sco X-1 using a dedicated pipeline that assumes a continuous wave model for the gravitational radiation emitted by the neutron star.

Second-generation gravitational wave detectors will have a broadband noise improvement by about a factor of 10. Using TwoSpect with data from second generation detectors will probe even deeper and wider regions of parameter space. Although originally developed for an all-sky search, the core TwoSpect pipeline could be tuned to be

used as a directed search method for known binary systems with poorly constrained orbital parameters.

ACKNOWLEDGMENTS

The authors gratefully acknowledge the support of the United States National Science Foundation for the construction and operation of the LIGO Laboratory; the Science and Technology Facilities Council of the United Kingdom, the Max-Planck-Society, and the State of Niedersachsen/Germany for support of the construction and operation of the GEO600 detector; and the Italian Istituto Nazionale di Fisica Nucleare and the French Centre National de la Recherche Scientifique for the construction and operation of the Virgo detector. The authors also gratefully acknowledge the support of the research by these agencies and by the Australian Research Council, the International Science Linkages program of the Commonwealth of Australia, the Council of Scientific and Industrial Research of India, the Istituto Nazionale

di Fisica Nucleare of Italy, the Spanish Ministerio de Economía y Competitividad, the Conselleria d'Economia Hisenda i Innovació of the Govern de les Illes Balears, the Foundation for Fundamental Research on Matter supported by the Netherlands Organisation for Scientific Research, the Polish Ministry of Science and Higher Education, the FOCUS Programme of Foundation for Polish Science, the Royal Society, the Scottish Funding Council, the Scottish Universities Physics Alliance, the National Aeronautics and Space Administration, OTKA of Hungary, the Lyon Institute of Origins (LIO), the National Research Foundation of Korea, Industry Canada and the Province of Ontario through the Ministry of Economic Development and Innovation, the National Science and Engineering Research Council Canada, the Carnegie Trust, the Leverhulme Trust, the David and Lucile Packard Foundation, the Research Corporation, and the Alfred P. Sloan Foundation. This article has LIGO Document No. LIGO-P1300048.

-
- [1] B. P. Abbott *et al.*, *Rep. Prog. Phys.* **72**, 076901 (2009).
 [2] T. Accadia *et al.*, *JINST* **7**, P03012 (2012).
 [3] B. Abbott *et al.*, *Phys. Rev. D* **76**, 082001 (2007).
 [4] B. Abbott *et al.*, *Phys. Rev. D* **72**, 102004 (2005).
 [5] P. R. Brady and T. Creighton, *Phys. Rev. D* **61**, 082001 (2000).
 [6] B. Abbott *et al.*, *Phys. Rev. D* **77**, 022001 (2008).
 [7] B. Abbott *et al.*, *Phys. Rev. D* **79**, 022001 (2009).
 [8] B. P. Abbott *et al.*, *Phys. Rev. Lett.* **102**, 111102 (2009).
 [9] J. Abadie *et al.* (LIGO Scientific Collaboration and Virgo Collaboration), *Phys. Rev. D* **85**, 022001 (2012).
 [10] B. P. Abbott *et al.*, *Phys. Rev. D* **80**, 042003 (2009).
 [11] J. Aasi *et al.* (LIGO Scientific Collaboration and Virgo Collaboration), *Phys. Rev. D* **87**, 042001 (2013).
 [12] B. Abbott *et al.* (LIGO Scientific Collaboration), *Phys. Rev. D* **76**, 082003 (2007).
 [13] J. Abadie *et al.* (LIGO Scientific Collaboration and Virgo Collaboration), *Phys. Rev. Lett.* **107**, 271102 (2011).
 [14] P. Jaranowski, A. Królak, and B. F. Schutz, *Phys. Rev. D* **58**, 063001 (1998).
 [15] S. V. Dhurandhar and A. Vecchio, *Phys. Rev. D* **63**, 122001 (2001).
 [16] E. Goetz and K. Riles, *Classical Quantum Gravity* **28**, 215006 (2011).
 [17] S. van der Putten, H. J. Bulten, J. F. J. van den Brand, and M. Holtrop, *J. Phys. Conf. Ser.* **228**, 012005 (2010).
 [18] L. Bildsten, *Astrophys. J. Lett.* **501**, L89 (1998).
 [19] M. Vigelius and A. Melatos, *Mon. Not. R. Astron. Soc.* **395**, 1972 (2009).
 [20] M. Priymak, A. Melatos, and D. J. B. Payne, *Mon. Not. R. Astron. Soc.* **417**, 2696 (2011).
 [21] K. Wette, M. Vigelius, and A. Melatos, *Mon. Not. R. Astron. Soc.* **402**, 1099 (2010).
 [22] M. Vigelius and A. Melatos, *Mon. Not. R. Astron. Soc.* **395**, 1985 (2009).
 [23] M. Vigelius and A. Melatos, *Mon. Not. R. Astron. Soc.* **386**, 1294 (2008).
 [24] A. Melatos and D. J. B. Payne, *Astrophys. J.* **623**, 1044 (2005).
 [25] A. Reisenegger and A. Bonacic, *Phys. Rev. Lett.* **91**, 201103 (2003).
 [26] G. Ushomirsky, *AIP Conf. Proc.* **575**, 284 (2001).
 [27] R. N. Manchester, G. B. Hobbs, A. Teoh, and M. Hobbs, *Astron. J.* **129**, 1993 (2005).
 [28] A. Patruno and A. L. Watts, [arXiv:1206.2727](https://arxiv.org/abs/1206.2727).
 [29] J. Papaloizou and J. E. Pringle, *Mon. Not. R. Astron. Soc.* **184**, 501 (1978).
 [30] R. V. Wagoner, *Astrophys. J.* **278**, 345 (1984).
 [31] B. J. Owen, *Phys. Rev. D* **82**, 104002 (2010).
 [32] R. Adhikari, P. Fritschel, and S. Waldman, LIGO Technical Report No. T060156, 2006 (unpublished), <https://dcc.ligo.org/LIGO-T060156-v1/public>.
 [33] T. Accadia *et al.*, *J. Phys. Conf. Ser.* **203**, 012074 (2010).
 [34] M. Frigo and S. G. Johnson, *Proc. IEEE* **93**, 216 (2005).
 [35] S. D. Mohanty, *Classical Quantum Gravity* **19**, 1513 (2002).
 [36] R. B. Davies, *J. Roy. Stat. Soc. C Appl. Stat.* **29**, 323 (1980).
 [37] LIGO Scientific Collaboration, LALApps Repository, <https://www.lsc-group.phys.uwm.edu/daswg/projects/lalsuite.html>.
 [38] M. Galassi *et al.*, *GNU Scientific Library Reference Manual*, 3rd ed. (Network Theory Ltd, 2009), ISBN 0954612078.
 [39] LIGO Collaboration and Virgo Collaboration (unpublished).

- [40] J. Aasi *et al.*, *Classical Quantum Gravity* **29**, 155002 (2012).
- [41] W. H. Press, B. P. Flannery, S. A. Teukolsky, and W. T. Vetterling, *Numerical Recipes: The Art of Scientific Computing*, 2nd ed. (Cambridge University Press, Cambridge, England, 1992).
- [42] The period difference term also allows for orbital frequency harmonic confusion up to the third harmonic or subharmonic in each detector.
- [43] E. Goetz *et al.*, *Classical Quantum Gravity* **26**, 245011 (2009).
- [44] D. Steeghs and J. Casares, *Astrophys. J.* **568**, 273 (2002).
- [45] D. K. Galloway, S. Premachandra, D. Steeghs, T. Marsh, J. Casares, and R. Cornelisse, *Astrophys. J.* **781**, 14 (2014).
- [46] A. L. Watts, B. Krishnan, L. Bildsten, and B. F. Schutz, *Mon. Not. R. Astron. Soc.* **389**, 839 (2008).